Polytope Sector-Based Synthesis and Analysis of Microstructural Architectures With Tunable Thermal Conductivity and Expansion

Jonathan B. Hopkins[1]
Mechanical and Aerospace Engineering,
University of California, Los Angeles,
Los Angeles, CA 90095
e-mail: hopkins@seas.ucla.edu

Yuanping Song
Mechanical and Aerospace Engineering,
University of California, Los Angeles,
Los Angeles, CA 90095
e-mail: adamsong@ucla.edu

Howon Lee
Mechanical and Aerospace Engineering,
Rutgers, The State University of New Jersey,
Piscataway, NJ 08854
e-mail: howon.lee@rutgers.edu

Nicholas X. Fang
Mechanical Engineering,
Massachusetts Institute of Technology,
Cambridge, MA 02139
e-mail: nicfang@mit.edu

Christopher M. Spadaccini
Materials Engineering Division,
Lawrence Livermore National Laboratory,
Livermore, CA 94550
e-mail: spadaccini2@llnl.gov

Polytope Sector-Based Synthesis and Analysis of Microstructural Architectures With Tunable Thermal Conductivity and Expansion

The aim of this paper is to (1) introduce an approach, called polytope sector-based synthesis (PSS), for synthesizing 2D or 3D microstructural architectures that exhibit a desired bulk-property directionality (e.g., isotropic, cubic, orthotropic, etc.), and (2) provide general analytical methods that can be used to rapidly optimize the geometric parameters of these architectures such that they achieve a desired combination of bulk thermal conductivity and thermal expansion properties. Although the methods introduced can be applied to general beam-based microstructural architectures, we demonstrate their utility in the context of an architecture that can be tuned to achieve a large range of extreme thermal expansion coefficients—positive, zero, and negative. The material-property-combination region that can be achieved by this architecture is determined within an Ashby-material-property plot of thermal expansion versus thermal conductivity using the analytical methods introduced. These methods are verified using finite-element analysis (FEA) and both 2D and 3D versions of the design have been fabricated using projection microstereolithography. [DOI: 10.1115/1.4032809]

Keywords: microstructural architectures, microarchitectured materials, cellular materials, thermal expansion, thermal conductivity, analytical optimization

1 Introduction

The ability to control the microarchitecture of repeating unit cells within large periodic lattices enables designers to custom-engineer new materials that achieve naturally unobtainable combinations of bulk properties. Such materials are often called microstructural architectures, periodic cellular solids [1], or microarchitectured materials [2]. An example of a 2D microstructural architecture that can achieve an unnaturally large negative thermal expansion effect (i.e., it substantially contracts when subject to an increase in temperature) is shown in Fig. 1(*a*). This architecture's topology was designed by Hopkins et al. in a previous publication [3] but will be used frequently as a case study for the purposes of this paper. The repeating unit cells of this microstructural architecture consist of three phases (i.e., void space and two solid constituent materials that possess different thermal expansion coefficients labeled α_1 and α_2 in the figure). Each unit cell possesses four tabs that connect to neighboring cells. If α_1 and α_2 are both positive and $\alpha_2 > \alpha_1$, the corners of each cell will expand into their surrounding void space (e.g., the labeled void space shown blue in Fig. 1(*a*)) and the tabs will be pulled inward by the angled red struts, which possess the larger expansion coefficient, as the architecture's temperature increases as shown in Fig. 1(*b*). Thus, the bulk material will exhibit an effective negative thermal expansion coefficient. If the geometric parameters within the microstructural architecture are changed, the same baseline topology can be tuned to possess near zero or even small positive thermal expansion coefficients. Furthermore, if the two materials are inverted within the architecture, the bulk material will exhibit a large positive thermal expansion coefficient. Thus, the architecture shown in Fig. 1(*a*) can be tuned to achieve a large range of desired thermal expansion coefficients.

Designing such microstructural architectures that are suited for practical use (e.g., they are 3D or exhibit isotropic properties) and achieve a specific combination of thermal properties for a particular application is a difficult task. Note that the microstructural architecture example in Fig. 1(*a*) is 2D and exhibits cubic properties only. The purpose of this paper directly addresses these issues. First, the paper introduces an approach, called PSS, which enables the synthesis of symmetric sectors within space-filling polytopes that constitute the periodic unit cells of 2D or 3D beam-based (i.e., trussed) microstructural architectures like the kind shown in Fig. 1(*a*) such that they achieve desired material property directionality (e.g., isotropic, cubic, orthotropic, etc.). Second, this paper provides closed-form analytical methods for enabling the analysis and optimization of these microstructural architectures such that the geometry of their synthesized topology can be optimally tuned to achieve a desired combination of thermal expansion and thermal conductivity properties. These methods can also be used to rapidly generate the material-property-combination boundaries achieved by the topologies of general microstructural architectures within the Ashby material selection chart [4] shown in Fig. 2. Note that the region colored a mixture of red and gray in this chart represents the combination of achievable thermal properties that the baseline topology of the microstructural architecture of Fig. 1(*a*) can achieve if its frame, shown gray and labeled α_1 in Fig. 1(*a*), is made of aluminum and its struts, shown red and labeled α_2, are made of acrylonitrile butadiene styrene (ABS). The property combination values that constitute this region were

[1]Corresponding author.

Contributed by the Design Automation Committee of ASME for publication in the JOURNAL OF MECHANICAL DESIGN. Manuscript received March 17, 2015; final manuscript received January 26, 2016; published online March 11, 2016. Assoc. Editor: James K. Guest.

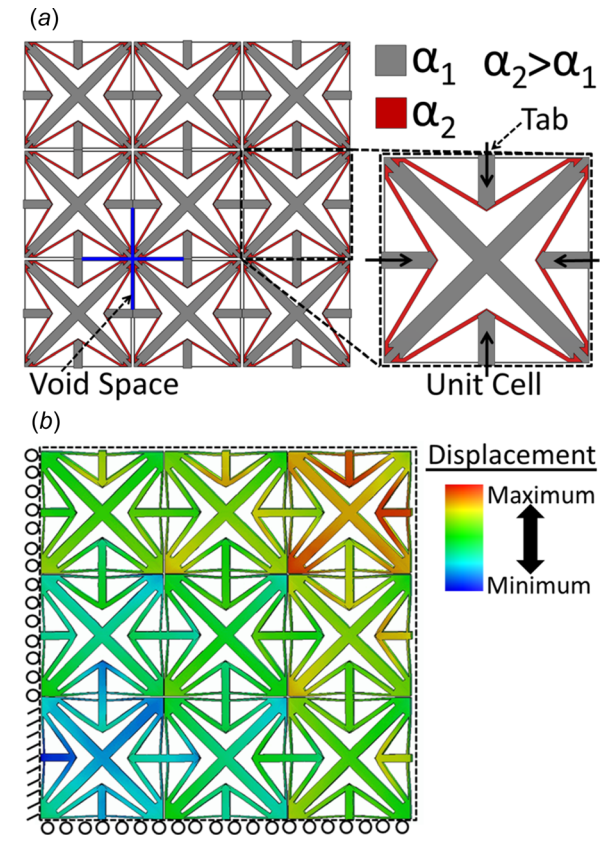

Fig. 1 A 2D microstructural architecture example that achieves tunable thermal expansion (*a*) and the same architecture shown deformed when subject to an increase in temperature (*b*)

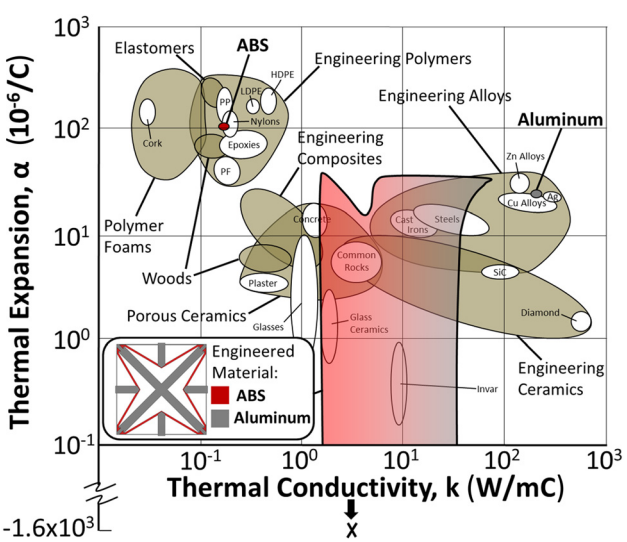

Fig. 2 Thermal expansion versus thermal conductivity Ashby chart

calculated using the theory of this paper by varying the geometric parameters within the microstructural architectures topology of Fig. 1(*a*) (i.e., the thicknesses and lengths of its beam elements).

The ability to engineer a material with a desired thermal expansion and thermal conductivity is important for applications that are subject to both spatial and time-dependent changes in temperature. Precision engineers, for instance, prefer to build flexure-based motion stages using materials with low thermal expansion but high thermal conductivity. The reason for this preference is that materials with low thermal expansion will not cause the system's stage to drift appreciably from its intended location due to the expansion or contraction of its flexure elements when ambient temperatures fluctuate. Additionally, materials with high thermal conductivity will rapidly distribute the heat generated from various sources (e.g., heat from the system's voice coil actuators) throughout the entire system so that all portions of the system are subject to a similar change in temperature. In this way, if the system is symmetric and does expand or contract due to a change in temperature, the system will do so the same amount everywhere and will thus experience minimal thermal drift error. There are many applications where engineers desire a material with near-zero thermal expansion or near-zero thermal conductivity. Materials that do not appreciably expand or contract when subject to changes in temperature would not be subject to thermal vibrations. Satellites, which are periodically exposed to or shielded from the direct rays of the sun, experience such damaging vibrations [5]. Materials with low thermal conductivity find applications in refrigeration, cryogenics, and the insulation of building, aircrafts, and submarines. Finally, if a material is joined to another material in a temperature changing environment, the bond between the two materials will likely not fail due to thermal property mismatches if one of the materials is engineered to achieve the same thermal conductivity and expansion as the material to which it is joined.

The topologies of other tunable thermal expansion microstructural architectures have been synthesized and optimized using alternative approaches prior to this paper. Sigmund and Torquato [6–8] generated a variety of tunable thermal expansion microstructural architecture designs using topology optimization. One of their optimized designs [8] is encouragingly similar to the design of Fig. 1(*a*) except that (i) it does not possess the central trusslike crossbeams (shown gray in Fig. 1), (ii) it possesses additional high-expansion material (shown red in Fig. 1(*a*)) at its corners, and (iii) its features are more irregular and organic in appearance. Chen et al. [9] also used topology optimization to generate another variation of this design. They were able to fabricate a 2D 5×5 lattice of their design with half-inch unit cells using direct metal deposition. Others have successfully synthesized significantly different designs using analytical equations tailored to those designs. Lakes [10,11] created a variety of concepts that utilize straight or curved bimaterial beams that join together to form tunable thermal expansion microstructural architectures. Jefferson et al. [12] designed an isotropic fully compliant 2D design and characterized its performance. Steeves et al. [13] created both 2D and 3D microstructural architecture designs that achieve high stiffness while exhibiting near-zero thermal expansion. Their 2D design was recently fabricated using conventional microfabrication techniques by Yamamoto et al. [14].

Others have also used different analytical approaches to characterize the thermal conductivity of various cellular materials. These approaches are largely limited to two-phase materials that consist of porous, foamlike structures. Collishaw and Evans [15] summarize many of these approaches. Most of these approaches ignore the effects of radiation and convection within the material, but a select few approaches do consider the effect of radiation [16,17]. Others have calculated hard bounds on the thermal conductivity of such porous cellular materials [18,19]. More recent work has focused on characterizing the flow of heat within periodic trusslike materials more similar to the kind analyzed in this paper [20,21]. The uniqueness of the proposed approach of this paper will be discussed in detail in Sec. 3.

2 PSS

This section introduces an approach, called PSS, which guides designers in arranging synthesized symmetric sectors within space-filling polytopes that are the periodic unit cells of 2D or 3D microstructural architectures. When arranged correctly, these

polytopes enable the desired directionality (e.g., isotropic, cubic, orthotropic, etc.) of the architecture's bulk properties.

Note that each unit cell within the microstructural architecture of Fig. 1(*a*) consists of four identical triangular sectors. One of these sectors is highlighted yellow in Fig. 3(*a*).The symmetric topology within this sector was synthesized using the freedom, actuation, and constraint topologies (FACT) approach [3], which utilizes a comprehensive library of geometric shapes that represent the mathematics of screw theory. These shapes, called freedom, actuation, and constraint spaces, enable designers to conceptualize the regions of space from which compliant elements (e.g., flexible beams, compliant hinges, and other elastic geometries) may be placed for achieving various bulk mechanical and thermal properties. In this way, designers can rapidly consider and compare a multiplicity of practical sector topologies before selecting the final sector that is most promising for achieving the desired bulk properties within the overall lattice of unit cells.

The detailed steps of the FACT approach and a discussion of how these steps were used to synthesize the triangular sector of Fig. 3(*a*) and other similar sectors are provided in Ref. [3]. For the sake of completeness, however, we briefly summarize these steps in this paragraph. To synthesize a sector that achieves a desired thermal expansion coefficient, the desired tab kinematics when the sector is subject to a change in temperature must first be identified. For thermal expansion or contraction, a translation of the tab along its axis when the sector is heated is desired. Every freedom space within the FACT library of shapes that contains this translation should then be identified. Each of these freedom spaces uniquely links to a complementary constraint space that represents the region of space within which flexible constraint elements could exist that behave as viable flexure bearing solutions that would correctly guide the tab with the desired freedom space's kinematics. When the most promising freedom space has been identified, flexure-bearing elements should then be selected from within its complementary constraint space such that the elements are symmetrically arranged. In this way, these elements will not participate in actuating the tab when subject to a change in temperature but will guide the tab's desired freedom-space kinematics. Note that the flexure-bearing elements in the sector of Fig. 3(*a*) are the two thin gray flexure blades that define the side of the unit cell square. Once the desired flexure-bearing elements have been selected, the system's actuation space can be identified. From this space, designers can rapidly visualize the positions and orientations of viable actuation elements that (i) will fully constrain the sector such that it possesses no passive degrees-of-freedom (i.e., the sector will be a structure) and (ii) will displace the tab along its axis when subject to a change in temperature. Note that the actuation elements in the sector of Fig. 3(*a*) are the two red angled struts shown. Although this approach largely limits designers to consider the topologies of sectors that possess parallel configurations, the same steps and principles can be extended to enable sectors that are also serial and hybrid [22]. Thus, the FACT approach is comprehensive in that a finite number of viable freedom, actuation, and constraint space options exist that enable designers to consider every tab-based sector topology configuration that achieves tunable thermal expansion behavior.

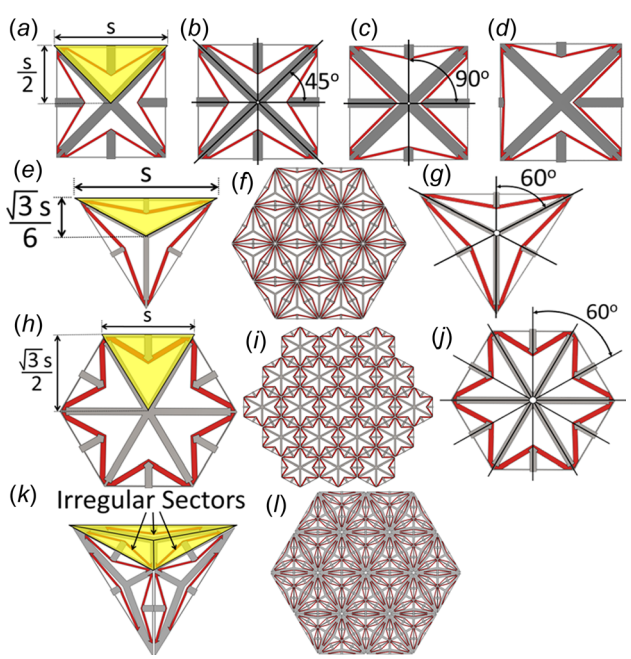

Fig. 3 Square unit cell with triangular sectors (*a*); cubic (*b*), orthotropic (*c*), and fully anisotropic (*d*) planes of symmetry; triangular unit cell with triangular sectors (*e*) and its lattice (*f*); the triangular cell possesses isotropic planes of symmetry (*g*); hexagonal unit cell with triangular sectors (*h*) and its lattice (*i*); the hexagonal cell possesses isotropic planes of symmetry (*j*); and irregular triangle sectors can be used within unit cells (*k*) to make lattices (*l*) with extreme thermal expansion properties

Although the unit cell shown in Fig. 3(*a*) would successfully achieve tunable thermal expansion behavior because of its FACT-synthesized sector, the bulk properties of the overall lattice would not be isotropic. As long as the repeating cells within periodic-lattice-based microstructural architectures are small compared with the overall size of the bulk lattice, it can be shown that the number, location, and orientation of the planes of symmetry within each unit cell can determine the directionality of the bulk material's properties [7,23]. The bulk properties of a large lattice that consists of the unit cell shown in Fig. 3(*b*) are cubic, for instance, because the cell possesses four planes of symmetry evenly spaced by 45 deg. If two different pairs of sectors were inserted into the square of the unit cell as shown in Fig. 3(*c*), the cell would possess only two planes of symmetry spaced 90 deg apart and would thus yield a lattice that is orthotropic. If four different sectors were inserted into the same square as shown in Fig. 3(*d*), the unit cell would possess no planes of symmetry and the lattice would be fully anisotropic. Thus, there is no way to insert the triangular sector of Fig. 3(*a*) into a square such that the resulting bulk lattice is isotropic.

There are, however, other regular polygons in which similar sectors can be inserted. Three similar sectors can, for instance, be inserted inside an equilateral triangle as shown in Fig. 3(*e*). The resulting unit cell can also fill space and can thus constitute a viable 2D lattice as shown in Fig. 3(*f*). This lattice is isotropic because its triangular unit cell possesses three planes of symmetry evenly spaced 60 deg as shown in Fig. 3(*g*) [23]. Note that although this condition is sufficient to produce isotropy, it is not a necessary condition for producing isotropy. When compared to a lattice consisting of the square unit cell in Fig. 3(*a*), a lattice consisting of the triangular unit cell in Fig. 3(*e*) can be made to achieve a larger negative thermal expansion effect because the triangular cell's side length, *s*, to sector depth ratio is larger than the square's.

As another example, consider the fact that six triangular sectors can also be inserted inside a regular hexagon as shown in Fig. 3(*h*). The resulting unit cell can also fill space and constitutes another viable 2D lattice as shown in Fig. 3(*i*). This lattice is also isotropic because its hexagonal unit cell possesses the three planes of symmetry evenly spaced 60 deg as well as three additional planes as shown in Fig. 3(*j*). When compared to the square unit cell in Fig. 3(*a*), a lattice consisting of the hexagonal unit cell in Fig. 3(*h*) cannot be made to achieve as large a negative thermal expansion effect because the hexagon's side length, *s*, to sector depth ratio is smaller than the square's.

Triangular sectors can also be inserted inside irregular polygons as well. Consider the isotropic triangular unit cell that consists of irregular triangular sectors shown in Fig. 3(*k*). A lattice consisting of these unit cells is shown in Fig. 3(*l*). By thinning its elements and inserting still more irregular triangular sectors inside the

irregular sectors, larger negative thermal expansion effects can be achieved. Theoretically, there are no limits on how many irregular sectors can be inserted inside each unit cell or on how large the negative thermal expansion effect can be made to achieve. Lakes showed that similar three-phase architectures can be made to achieve unbounded thermal expansion coefficients [24]. There are, however, obvious practical bounds on these limits that are determined in part by fabrication resolution capabilities or by the sizes of the constituent materials' grains, molecules, or atoms.

FACT can also be used to synthesize pyramidal sectors that are inserted within space-filling polyhedrons to achieve 3D microstructural architectures instead of using synthesized triangular sectors that are inserted within space-filling polygons as discussed previously for achieving 2D architectures. Consider the pyramidal sector shown in Fig. 4(*a*) with a square base. This sector was synthesized using the same steps of FACT discussed previously and is analogous to the 2D sector in Fig. 3(*a*). Six of the pyramidal sectors in Fig. 4(*a*) can be inserted inside a cube polyhedron that then becomes the repeating unit cell within a 3D microstructural architecture. This architecture's properties are cubic because its unit cell possesses the nine unique planes of symmetry spaced 45 deg on each square face as shown in Fig. 4(*b*) [23]. By inserting different versions of the same pyramidal sector into the unit-cell cube (similar to what was done with the 2D version in Figs. 3(*b*)–3(*d*)), the resulting bulk lattice in Fig. 4(*a*) can also be made orthotropic or fully anisotropic, but not isotropic. If 12 similar pyramidal sectors, each with a base shaped like a rhombus instead of a square (Fig. 4(*c*)), are inserted within a rhombic dodecahedron, another microstructural architecture is created that also possesses the same nine planes of symmetry shown in Fig. 4(*b*). Combinations of different space-filling polyhedrons (e.g., tetrahedrons combined with octahedrons) can also be used to achieve 3D microstructural architectures that possess desired material property directionality.

It may be possible to create isotropic 3D microstructural architectures by inserting FACT-synthesized irregularly shaped pyramidal sectors inside randomly generated space-filling polyhedrons. A 2D polygon version of this concept is shown in Fig. 4(*d*) to clarify how isotropy could be achieved using this concept. As long as all the interior angles within each randomly shaped polygon are less than 180 deg and the vertices of each polygon are all coincident with the vertices of other polygons (i.e., no vertex lies on the side or edge segment of a neighboring polygon), irregular triangular sectors (Fig. 4(*d*)) could be inserted inside each unit cell such that the tabs of one cell polygon will always join with the tabs of its neighboring cell polygons. The bulk properties of such lattices should approach isotropy the larger their lattice size is with respect to the size of their unit cell constituents. The reason is that the directionality of a lattice's properties is largely determined by the interactions that occur along the axes of these connecting tabs, and these tabs would be numerous and randomly oriented. In the case of the negative thermal expansion example of Fig. 4(*d*), each tab within the lattice would attempt to pull its neighboring cell inward along its randomly oriented axis when subject to an increase in temperature causing a statistically averaged uniform contraction of the lattice in all directions. The idea is inspired by natural materials that achieve isotropy because their inherently directional grains are randomly shaped and oriented such that the overall material's bulk properties are statistically averaged to be uniform in all directions [25].

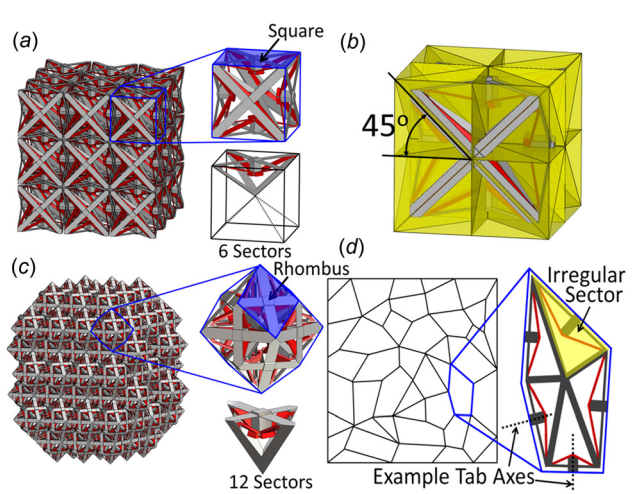

Fig. 4 A 3D lattice consisting of cube-shaped unit cells made of symmetric pyramidal sectors (*a*); its unit cells possess cubic planes of symmetry (*b*); a 3D lattice consisting of rhombic-dodecahedron-shaped unit cells also possesses cubic properties (*c*); and randomly shaped polytopes could produce isotropic bulk properties (*d*)

PSS is a two-step approach for synthesizing the topologies of microstructural architectures that achieve desired material property directionality. These steps are as follows:

Step 1: Use FACT to synthesize the symmetric topologies of triangular sectors for generating 2D architectures, or pyramidal sectors for generating 3D architectures that enable the desired bulk properties. It is important to note that every desired bulk property requires a different utilization of FACT's shapes. While the steps are detailed in Ref. [3] for using FACT's shapes to synthesize sectors that produce tunable thermal expansion coefficients like the sectors of this paper, the task of determining how FACT can be used to generate topologies that achieve other properties (e.g., negative Poisson's ratio, high strength-to-weight ratio, extreme ductility, thermally tunable elastic modulus, and desired damping properties) is ongoing.

Step 2: Insert the FACT-designed sectors within space-filling polygons for 2D architectures or space-filling polyhedrons for 3D architectures that behave as unit cells with the appropriate number, location, and orientation of planes of symmetry for producing the desired material property directionality according to the principles discussed in this section.

Projection microstereolithography [26,27] was used to fabricate the designs of this paper as near to their intended scales as possible. The 2D and 3D designs of Figs. 1 and 4(*a*) were fabricated using two differently polymers (i.e., hexanediol diacrylate for the frame and poly(ethylene glycol) diacrylate with red dye for the struts) as shown in Figs. 5(*a*) and 5(*b*), respectively.

3 Analytical Calculation Methods

This section provides the analytical methods used to calculate the thermal expansion and thermal conductivity of microstructural architecture topologies synthesized using PSS. These methods were used to generate the boundaries of the mixed red and gray region shown in Fig. 2. Although the methods of this section can be extended to enable the analysis of general microstructural architectures, these methods are provided here in the context of architectures made of a single repeating unit cell that (i) consists of rectangular-prism-shaped beam elements connected to arbitrarily shaped junction bodies at their ends, (ii) is joined with its neighboring cells by tabs similar to the cells shown in Fig. 1(*a*), (iii) possesses cubic planes of symmetry, (iv) is square- or cube-shaped, and (v) consists of constituent elements made of isotropic homogeneous linear-elastic materials. It is important to recognize that the effective lattice properties calculated using the methods of this section are, thus, orthotropic and correspond with the directions along the axes of the lattice's cell tabs. As an example case study, we will apply the methods of this section to the 2D microstructural architecture topology of Fig. 1(*a*) shown again in Fig. 6.

3.1 Thermal Expansion. This section reviews the analytical method provided in Ref. [3], which can be used to calculate the effective thermal expansion coefficient of a microstructural architecture that satisfies the conditions discussed in the introduction of

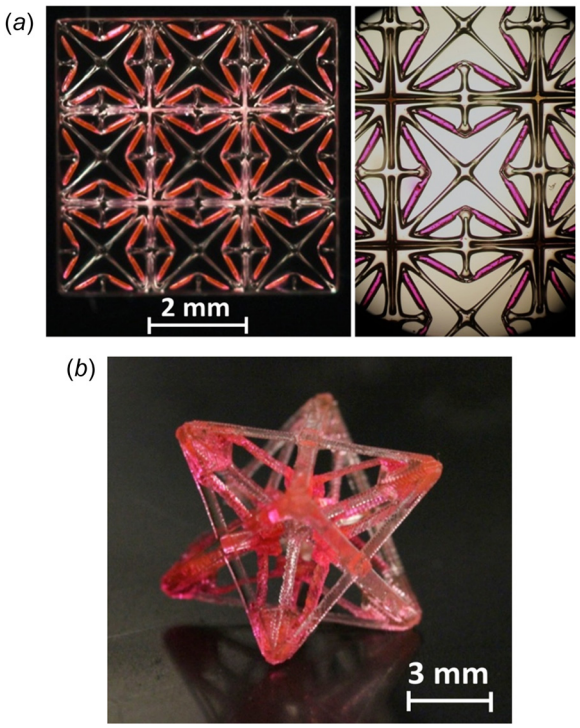

Fig. 5 2D (*a*) and 3D (*b*) microstructural architecture designs fabricated using projection microstereolithography

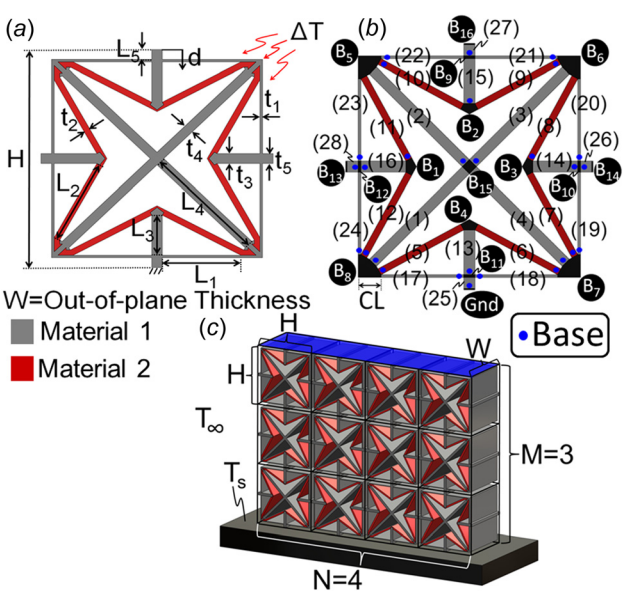

Fig. 6 Unit cell parameters (*a*), numbered elements and bodies (*b*), and lattice parameters (*c*)

Sec. 3. The thermal expansion of an entire lattice of unit cells, α_{lattice}, can be determined by calculating the downward tab displacement, d, of a single unit cell that is held fixed at its opposing end and subject to a change in temperature, ΔT, according to

$$\alpha_{\text{lattice}} = -\frac{(d/H)}{\Delta T} \tag{1}$$

where H is the tab-to-tab height of a single unit cell. Note that these parameters are labeled in Fig. 6(*a*). The tab displacement, d, can be calculated by applying the direct-stiffness-matrix method in the form provided by Hopkins et al. [3]. For this method, the areas shown black in the unit cell of Fig. 6(*b*) are modeled as rigid bodies (i.e., B_b) and the areas shown red and gray are modeled as compliant beams of different materials. The resulting translations and rotations of every rigid body in the cell can be calculated for a change in temperature, ΔT, using the following equation derived in Ref. [3]:

$$[\mathbf{T}_1 \quad \mathbf{T}_2 \quad \cdots \quad \mathbf{T}_\mathbf{R}]^{\mathrm{T}} = -[K]^{-1}\mathbf{A}\Delta T \tag{2}$$

The $\mathbf{T_b}$ vectors are 1×6 displacement twist vectors [28] that contain the necessary information to calculate the translations and rotations of each of the R rigid bodies labeled B_b in Fig. 6(*b*). Note that the unit cell in Fig. 6(*b*) possesses 16 rigid bodies ($R = 16$) and one fixed or grounded body labeled Gnd. The $[K]$ matrix in Eq. (2) is a $6R \times 6R$ stiffness matrix that can be constructed for any general beam-based structure according to the details provided in Ref. [3]. Similarly, $\mathbf{A}$ is a $6R \times 1$ thermal vector that can be constructed for similar structures according to the same reference.

3.2 Thermal Conductivity. This section provides the analytical method necessary to calculate the effective thermal conductivity of a microstructural architecture that satisfies the conditions discussed in the introduction of Sec. 3. As an example, we will calculate the effective thermal conductivity of the lattice in Fig. 6(*c*).

To calculate this lattice's effective thermal conductivity, we treat the lattice as a fin and set its tip temperature (i.e., the temperature at the top surface shown blue in Fig. 6(*c*)) equal to the tip temperature of another theoretical fin made of a solid homogenous material that possesses the effective thermal conductivity of the lattice. This theoretical fin must occupy the same volume as the lattice (i.e., $WNMH^2$ as shown in Fig. 6(*c*)) and must be subject to the same ambient conditions. The conditions imposed on the theoretical fin do not matter as long as they are the same conditions imposed on the lattice when finding its tip temperature. Thus, to simplify the mathematics necessary to determine the theoretical fin's tip temperature, we attach the fin at one end to a heat reservoir with a sustained surface temperature of T_s and insulate the fin's other end, shown as the blue surface in Fig. 6(*c*), such that it is adiabatic. We also immerse the fin in a fluid with a convection coefficient of h_c and a sustained temperature of T_∞. We assume steady-state conditions and one-dimensional conduction [29] along the theoretical fin's length because, typical of most solid homogenous fins, temperature changes in the longitudinal direction are much larger than those in the transverse directions. Thus, under these conditions, the theoretical fin's tip temperature, T_{tip}, can be calculated according to [29]

$$T_{\text{tip}} = \left(\frac{1}{\cos h(mMH)}\right) \cdot (T_s - T_\infty) + T_\infty \tag{3}$$

where m is the classic fin parameter [29] defined by

$$m = \sqrt{\frac{h_c(2NH + 2W)}{k_{\text{lattice}}(NHW)}} \tag{4}$$

where k_{lattice} is the theoretical fin's thermal conductivity. Recall that this thermal conductivity is the same as the lattice's effective thermal conductivity as long as the theoretical fin's tip temperature is set equal to the lattice's tip temperature when the lattice is subject to the same ambient conditions. Note from Fig. 6(*c*) that $(2NH + 2W)$ in the numerator of Eq. (4) is the fin's perimeter and (NHW) in the denominator of Eq. (4) is the fin's cross-sectional area. By reorganizing Eqs. (3) and (4), the lattice's effective thermal conductivity, k_{lattice}, can be calculated according to

$$k_{\text{lattice}} = 2h_c\left(\frac{1}{W}+\frac{1}{NH}\right)\cdot\left(MH/a\cos h\left(\frac{T_s-T_\infty}{T_{\text{tip}}-T_\infty}\right)\right)^2 \quad (5)$$

To calculate the lattice's effective thermal conductivity using Eq. (5), the lattice's tip temperature, T_{tip}, must be determined for the conditions specified previously. To do this, the lattice is treated as a network of interconnected beam elements that each behave as an individual fin. By recognizing that the steady-state temperature profiles of each beam element within one column of unit cells is the same as the temperature profiles of corresponding beam elements in neighboring columns of unit cells, these temperature profiles can be calculated by considering only a single column of cells from within the lattice. The reason for this observation is that the lattice's columns of unit cells connect together by tabs that do not experience conductive heat transfer (i.e., they are adiabatic across the surface where they join) because their connecting bodies are always the same temperature due to symmetry. The only exception to this observation occurs at the tabs along the two far sides of the lattice that do not connect to neighboring columns of cells. The exposed surfaces of these tabs would experience convective heat transfer, which would not be accounted for using the approach proposed here. The effect of this heat transfer on the steady-state temperature profiles of most elements in the bulk lattice would, however, be negligible as long as the surface area at the end of these tabs is comparably small and the lattice possesses a large number of cell columns.

The lattice's tip temperature can be calculated by considering only one column of cells from within a larger lattice. As an example, consider the column of cells from the lattice in Fig. 6(*c*) shown in Fig. 7(*a*). As long as this column represents a typical column that is sandwiched between two other identical neighboring columns within the lattice, one can assume that the temperature of bodies B_{13} and B_{14} (labeled in Fig. 7(*a*)) are the same, the temperature of bodies B_{29} and B_{30} are the same, and the temperature of bodies B_{45} and B_{46} are the same due to symmetry. Thus, no heat transfer occurs at the bodies labeled B_{13}, B_{14}, B_{29}, B_{30}, B_{45}, and B_{46}. Note also that the body labeled Gnd in Fig. 7(*a*) has a temperature of T_s and no heat transfer occurs at the body labeled B_{48} because of the ambient conditions imposed on the lattice as shown in Fig. 6(*c*). The labeling convention used to number the bodies and elements of the example in Fig. 7(*a*) is established by Fig. 6(*b*). In this figure, bodies are labeled B_b, where b is the number assigned to that body, and elements are labeled (e), where e is the number assigned to that element. The bodies and elements within the first unit cell in the column of Fig. 7(*a*) correspond directly with the labeled numbers provided in Fig. 6(*b*). To determine the correct number assigned to bodies within subsequent unit cells in the stacked column numbered i, where the first unit cell corresponds with $i=1$, one can use $b+16(i-1)$, where b is the number of the corresponding body in the first unit cell labeled in Fig. 6(*b*). Note that there are 16 bodies in each unit cell. The body labeled Gnd is associated with a $b=0$. To determine the correct number assigned to elements within subsequent unit cells in the stacked column numbered i, one can use $e+28(i-1)$, where e is the number of the corresponding element in the first unit cell labeled in Fig. 6(*b*). Note that there are 28 elements in each unit cell.

The one-dimensional temperature profile along the length of each element, $T_{(e)}(x)$, within the column of unit cells in Fig. 7(*a*) can be calculated by assuming each element behaves as a fin according to [29]

$$T_{(e)}(x) = C_{1(e)}e^{m_{(e)}x} + C_{2(e)}e^{-m_{(e)}x} + T_\infty \quad (6)$$

where x is the distance from one end of the element to the other end along its length. The blue dots in Fig. 6(*b*) establish the convention pertaining to which end of the elements corresponds with their base (i.e., where $x=0$). Note that it does not matter which end of each element is assigned a blue dot as long as the convention established is maintained throughout the calculation. The values $C_{1(e)}$ and $C_{2(e)}$ are unknown constants that pertain to element (e), and $m_{(e)}$ is the same element's fin parameter [29] defined by

$$m_{(e)} = \sqrt{\frac{h_c P_{(e)}}{k_{(e)}A_{c,(e)}}} \quad (7)$$

where $P_{(e)}$ is the cross-sectional perimeter of element (e), $k_{(e)}$ is the element's thermal conductivity, and $A_{c,(e)}$ is its cross-sectional area.

To determine the temperature profile of any element (e) within the column of unit cells in Fig. 7(*a*), we need to determine the element's unknown constants $C_{1(e)}$ and $C_{2(e)}$ in Eq. (6). To do this, we must solve for all the elements' unknown constants within the column of unit cells simultaneously by defining a sufficient number of boundary condition equations. Note that we need to define as many boundary condition equations as there are unknown constants (i.e., two for every element in the column of cells or $56M$ where $M=3$ in Fig. 7(*a*)) to achieve our objective. We have already identified a few of these boundary condition equations

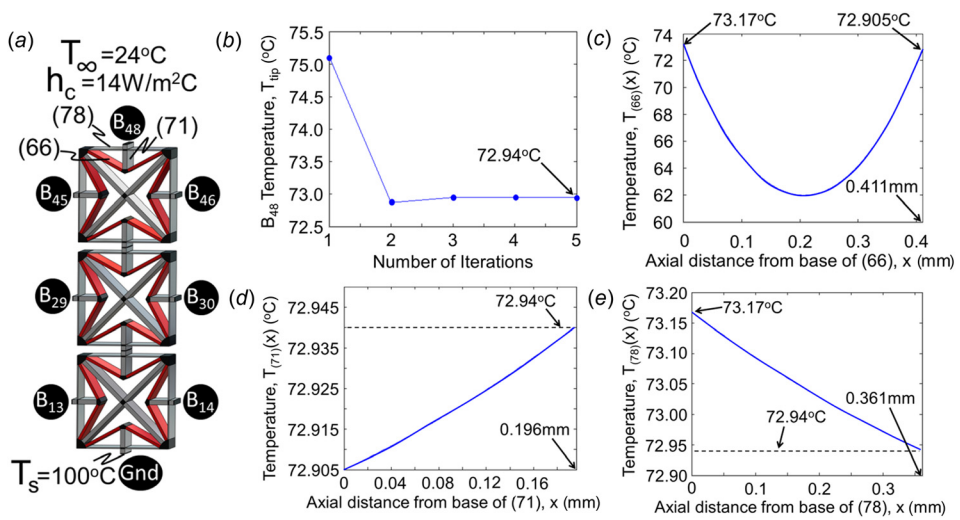

Fig. 7 Single column within the lattice of Fig. 6(*c*) (*a*); tip temperature calculated iteratively (*b*); and temperature profiles in element (66) (*c*), element (71) (*d*), and element (78) (*e*)

previously. Recall that the body labeled Gnd in Fig. 7(*a*) possesses a temperature of T_s, and thus, the base of element (25), shown in Fig. 6(*b*), must also possess this temperature (i.e., $T_{(25)}(0) = T_s$). Furthermore, recall that no heat transfer occurs at the bodies labeled B_{13}, B_{14}, B_{29}, B_{30}, B_{45}, B_{46}, and B_{48}. Thus, by recognizing that the conductive heat transfer rate (i.e., the energy flow per unit time) at any distance x from the base of an element (e) along its length is [29]

$$\dot{Q}_{\text{cond},(e)}(x) = -k_{(e)}A_{c,(e)}\left(\frac{dT_{(e)}(x)}{dx}\right) \tag{8}$$

the labeling convention in Fig. 6(*b*) can be used to establish seven more boundary condition equations as follows:

$$\begin{aligned}\dot{Q}_{\text{cond},(28)}(L_5) &= \dot{Q}_{\text{cond},(26)}(L_5) = \dot{Q}_{\text{cond},(56)}(L_5) \\ &= \dot{Q}_{\text{cond},(54)}(L_5) = \dot{Q}_{\text{cond},(84)}(L_5) \\ &= \dot{Q}_{\text{cond},(82)}(L_5) = \dot{Q}_{\text{cond},(83)}(L_5) = 0\end{aligned} \tag{9}$$

Recall that L_5 is the length of each tab labeled in Fig. 6(*a*). The remaining necessary boundary condition equations for solving each element's unknown constants can be established at the lattice's junction bodies, shown black in Fig. 6(*b*). If we assume that each of these bodies possesses a uniform temperature at all points throughout its geometry, the temperatures at the ends of the elements that join to each body can be set equal to each other. As an example, consider body B_5, labeled in Fig. 6(*b*). If we assume that this body possesses the same temperature at all points throughout its geometry, an additional four independent boundary condition equations can be established as follows:

$$T_{(23)}(L_1) = T_{(11)}(L_2) = T_{(2)}(L_4) = T_{(10)}(0) = T_{(22)}(0) \tag{10}$$

Recall that L_1, L_2, and L_4 are labeled in Fig. 6(*a*). By applying the same principle to the remaining bodies within the column of unit cells in Fig. 7(*a*), an additional 115 independent boundary condition equations can be established.

A final set of boundary condition equations can be established by applying the first law of thermodynamics to each junction body within the column of unit cells. As an example, consider again body B_5 labeled in Fig. 6(*b*). By equating the heat transfer rate in and out of this body, another boundary condition can be established according to

$$\begin{aligned}&\dot{Q}_{\text{cond},(23)}(L_1) + \dot{Q}_{\text{cond},(11)}(L_2) + \dot{Q}_{\text{cond},(2)}(L_4) \\ &\quad = \dot{Q}_{\text{cond},(10)}(0) + \dot{Q}_{\text{cond},(22)}(0) + \dot{Q}_{\text{conv},5}\end{aligned} \tag{11}$$

where

$$\dot{Q}_{\text{conv},b} = h_c A_{s,b}(T_b - T_\infty) \tag{12}$$

and where $A_{s,b}$ is the exposed surface area of the junction body labeled B_b in Fig. 6(*b*), and T_b is the temperature of the same body. Note that $b = 5$ in Eq. (11) and that the blue dots assigned for the convention of Fig. 6(*b*) determines which side of Eq. (11) an element's conductive heat transfer rate belongs. By applying the first law of thermodynamics in this way to the remaining bodies within the column of unit cells in Fig. 7(*a*), the final 40 independent boundary condition equations can be established.

Thus, using the previously mentioned boundary condition equations, each element's unknown constants, $C_{1(e)}$ and $C_{2(e)}$ in Eq. (6), from within the column of unit cells in Fig. 7(*a*) can be calculated. To do this, the system of equations must be solved iteratively. For the first iteration, we assume that each body does not experience convective heat transfer (e.g., the last term in Eq. (11) is set to zero). Under this condition, preliminary values for the $C_{1(e)}$ and $C_{2(e)}$ constants from Eq. (6) can be calculated for each element without knowing each body's temperature, T_b. Then, using these preliminary values, the temperature of each body (including the desired tip temperature, T_{tip}, of body B_{48} labeled in Fig. 7(*a*)) can be calculated by finding the temperatures at the ends of each element. For body B_{48}, this temperature is $T_{(83)}(L_5)$. With these body temperatures, the convective heat transfer of each body can then be considered using equations similar to Eq. (11) to find more accurate values for the constants $C_{1(e)}$ and $C_{2(e)}$. By iterating this process until the temperature calculated at each body stabilizes, the lattice's effective thermal conductivity, k_{lattice}, in Eq. (5) can be determined using the stabilized tip temperature, T_{tip}.

The calculated tip temperature of a 3×4 lattice of unit cells (Fig. 6(*c*)) with the geometric parameters and material properties specified in Table 1 is plotted in Fig. 7(*b*) verses the number of iterations used to calculate the temperature using this approach. Note that the tip temperature stabilizes to its final value of 72.94 °C after only a few iterations. This final value represents the steady-state temperature at the insulated surface, shown blue in Fig. 6(*c*), when the lattice is placed on a hot surface with a temperature of $T_s = 100$ °C in a still air environment with a convection coefficient of $h_c = 14$ W/m^2 C and an ambient temperature of $T_\infty = 24$ °C (i.e., room temperature). By inserting this final tip temperature into Eq. (5), the lattice's effective thermal conductivity is calculated to be $k_{\text{lattice}} = 12.64$ W/m C. The plot shown in Fig. 7(*b*) shows iterations only until the lattice's effective thermal conductivity stopped changing with a magnitude greater than 0.0001 W/m C for each iteration. The stabilized steady-state temperature profiles, $T_{(e)}(x)$, along the lengths of three sample elements, (66), (71), and (78), starting at $x = 0$ from the ends with the blue dots in Fig. 6(*b*), are plotted in Figs. 7(*c*)–7(*e*). Note that the lowest steady-state temperature in the lattice occurs near the middle of the uppermost ABS struts (i.e., elements (66) and (65) at ~62 °C).

It is interesting to note that a lattice's effective thermal conductivity is not only dependent on the geometric parameters and material properties of its constituent elements (like those specified in Table 1) but also dependent on its ambient conditions, the number of constituent cell rows and columns, and its scale factor. For a lattice immersed in a fluid and sandwiched between a thermally conductive surface and an insulated surface, like the one shown in Fig. 6(*c*), with the additional parameters specified in the caption of Fig. 8, a plot showing the lattice's effective thermal conductivity as a function of scale factor is provided in Fig. 8(*a*). Note that the lattice's thermal conductivity remains largely constant for unit cells smaller than 1 mm. Four other plots showing the same lattice's effective thermal conductivity as a function of (i) the convection coefficient of its ambient fluid, h_c, (ii) the lattice's out-of-plane thickness, W, (iii) the number of unit cell columns along the conductive surface, N, and (iv) the number of unit cell rows away from the conductive surface, M, are provided in Figs. 8(*b*)–8(*e*). The lattice's effective thermal conductivity is not dependent on the temperature of the conductive surface, T_s, or on the

Table 1 Example parameters defined in Fig. 6(*a*)

Geometric parameters		Material 1 (aluminum)	Material 2 (ABS)
H	1.000 mm	Young's modulus	Young's modulus
t_1	0.012 mm	$E = 68$ GPa	$E = 1.4$ GPa
L_1	0.361 mm	Shear modulus	Shear modulus
t_2	0.029 mm	$G = 25$ GPa	$G = 0.483$ GPa
L_2	0.411 mm	Thermal expansion	Thermal expansion
t_3	0.049 mm	$\alpha = 24 \times 10^{-6}$ (1/°C)	$\alpha = 100 \times 10^{-6}$ (1/°C)
L_3	0.196 mm	Density	Density
t_4	0.044 mm	$\rho = 2698.9$ kg/m^3	$\rho = 1060$ kg/m^3
L_4	0.573 mm	Thermal conductivity	Thermal conductivity
t_5	0.049 mm	$k = 210$ W/m C	$K = 0.179$ W/m C
L_5	0.015 mm		
W	0.020 mm		

temperature of the ambient fluid, T_∞. It is important, however, when calculating a lattice's thermal conductivity that the difference between the temperature of the conductive surface and the ambient fluid be made sufficiently large to ensure that the temperature at the tip, T_{tip}, does not reach the ambient fluid's temperature at steady state.

Some of the assumptions inherent to the analytical method of this section can produce nontrivial calculation errors when determining the effective thermal conductivity of microstructural architectures with geometric parameters that violate certain conditions. If, for instance, the out-of-plane thickness, W, of the lattice in Fig. 6(*c*) is large enough, pockets of stagnant fluid would exist between the elements that would possess temperatures with values different from the fluid's far-field temperature, T_∞. Thus, the effective lattice's thermal conductivity calculated using the method of this section would become increasingly inaccurate for a larger and larger out-of-plane thickness (Fig. 8(*c*)) because this method assumes that the ambient fluid's temperature remains the same everywhere. The convection coefficient, h_c, is also assumed to be constant everywhere. Note also that similar to most methods used to calculate the thermal conductivity of cellular materials, the method of this section does not consider the effect of radiation heat transfer from nearby elements within the lattice. Adding this effect to the method provided in this section is the topic of future work. Recall also that this method assumes that the temperature of each body or node (shown black in Fig. 6(*b*)) within the lattice is uniform throughout its geometry regardless of its size and shape (i.e., we assume that the thermal conductivity of each junction body is infinitely large). In actuality, however, these bodies would possess their own nonconstant temperature profiles across their geometries. Thus, the larger a lattice's junction bodies are, the less accurate the analytical method of this section is at calculating the lattice's effective thermal conductivity. Note also that regardless of how small these bodies are in comparison with the overall lattice's cell size, our assumption always produces a finite calculation error in the lattice's effective thermal conductivity that is further compounded as more and more cells are stacked in series within the lattice. Thus, the fewer cell rows that exist within a microstructural architecture (i.e., the smaller the M is), the more accurate the method of this section is. For most lattice-based designs with sufficiently small junction bodies, however, these sources of error are generally insignificant except for large lattices or 2D designs with large out-of-plane thicknesses.

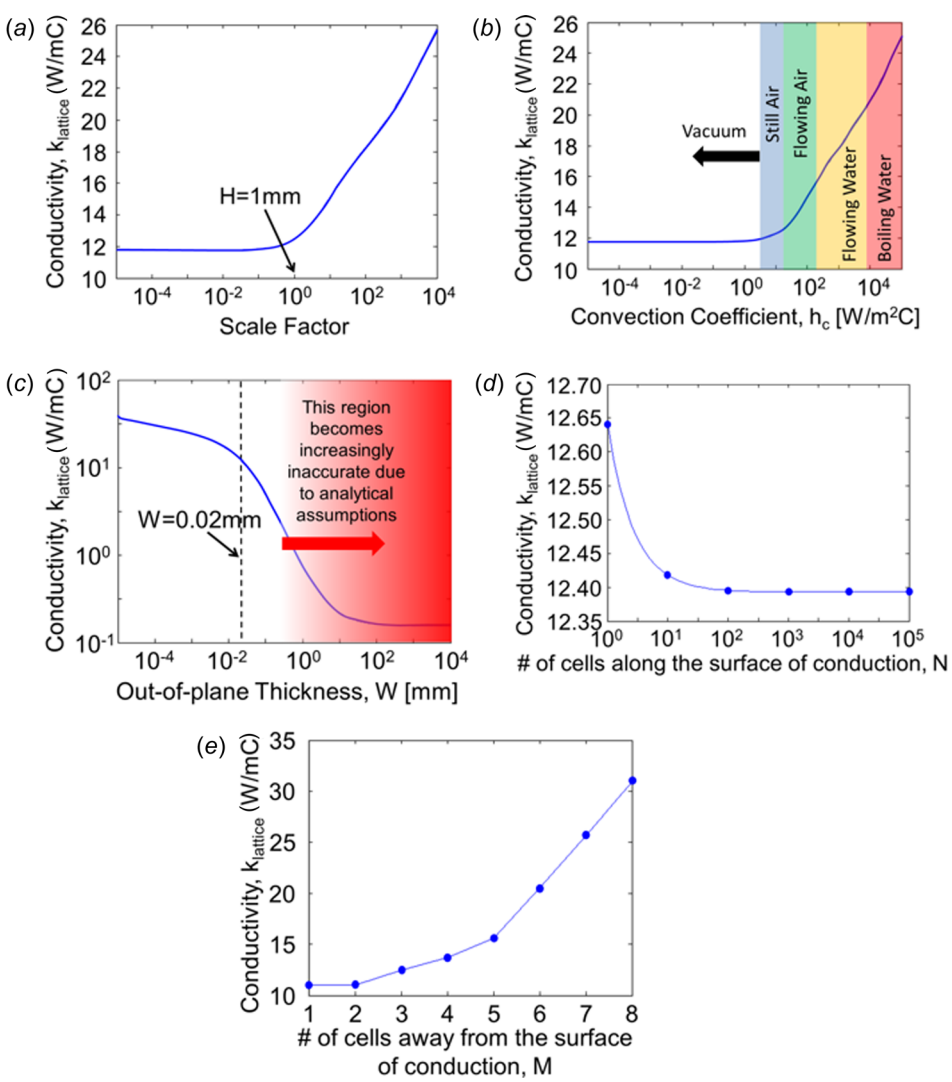

Fig. 8 Thermal conductivity versus scale factor (*a*), convection coefficient (*b*), out-of-plane thickness (*c*), number of cell columns (*d*), and number of cell rows (*e*); unless otherwise specified, these plots were generated for a lattice with the parameters specified in Table 1 and with a scale factor = 1, $N = 4$, $M = 3$, and $h_c = 14\ \mathrm{W/m^2\ C}$

3.3 Generating Property Combination Regions. This section explains how the analytical methods of Secs. 3.1 and 3.2 can be used to determine the property combination region within the Ashby chart of Fig. 2 for a microstructural architecture that satisfies the conditions discussed in the introduction of Sec. 3. To generate such a region, these analytical methods can be used to calculate both the thermal expansion and thermal conductivity of the architecture's lattice for every version of the design's topology that is geometrically compatible. Thus, by sweeping through all the lattice's possible geometric parameters, points can be plotted within the chart of Fig. 2 that define the desired region.

The boundary of the mixed red and gray region shown in Fig. 2 was determined in this way using the cell topology of Fig. 6(*a*) with the constituent material properties given in Table 1 for aluminum and ABS. Constraints were placed on some of the geometric parameters to ensure that the analytical method calculated accurate results and to reduce the number of independent variables for decreasing the time it took to calculate all of the results. The imposed constraints include the following: (i) Parameter t_3 was set equal to parameter t_5. (ii) Parameter H was set equal to 1 mm. (iii) Parameter L_5 was set equal to ~1.5% of H. (iv) Parameter W was set equal to 2% of H. (v) Parameters t_3, t_4, and CL (labeled in Fig. 6(*b*)) were not allowed to be larger than 10% of H to ensure that no rigid body labeled B_b in Fig. 6(*b*) could become large enough to cause the calculated results to be unacceptably inaccurate. Six of the remaining independent parameters were then varied from 0.2% of H to the largest size that was geometrically compatible within the topology's design (i.e., no element's geometry should overlap or collide with the geometry of any other element or junction body in the design) using resolution increments of 0.5% of H. In this way, the thermal expansion, α_{lattice}, and thermal conductivity, k_{lattice}, of 949,240 viable different design instantiations of the lattice topology shown in Fig. 6(*c*) were plotted using MATLAB as shown in Fig. 9. Note that a lattice size of $N = 4$ and $M = 3$ was used to calculate their effective thermal conductivity values, as well as a scale factor = 1 and an ambient convection coefficient of $h_c = 14\ \text{W/m}^2\ \text{C}$. The plot in Fig. 9(*a*) provides the effective properties of the design instantiations with positive thermal expansion coefficients, and the plot of Fig. 9(*b*) provides the effective properties of design instantiations with negative thermal expansion coefficients. Note the similarities between the shape of the plot in Fig. 9(*a*) and the mixed red and gray region shown in Fig. 2.

Finally, note that the boundary of the region in Fig. 2 is conservative as it pertains to the microstructural architecture lattice of Fig. 6(*c*). If the constraints listed in the previous paragraph had been relaxed such that more independent parameters (e.g., W or L_5) had been allowed to be varied, this region would likely encompass a larger area. In addition, if every parameter had been varied using smaller increments that start from a smaller initial value, this region would likely be even larger. Furthermore, if the analytical methods of this section had been advanced such that fewer assumptions are made about lattice's junction bodies, the limits placed on t_3, t_4, and CL could also have been relaxed such that an even larger region within the plots of Figs. 2 and 9 could have been calculated.

4 Finite Element Verification

In this section, we use an FEA software package (i.e., COMSOL) to verify the theory provided in Sec. 3.2. The theory reviewed in Sec. 3.1 has already been verified in a previous publication [3].

We use FEA to analyze the temperature profile within the topology of a unit cell design shown in Fig. 10(*a*). Its geometric parameters, labeled in Fig. 6(*a*), are provided in Fig. 10(*a*). Its gray frame is aluminum and its red struts are ABS with the same properties provided in Table 1. If the effects of radiation heat transfer are ignored, the bottom tab surface, T_s, is set equal to 100 °C, the outermost faces of the other three tabs are set to be adiabatic for the reasons discussed in Sec. 3.2, and the unit cell is immersed in still air with a convection coefficient, h_c, of $14\ \text{W/m}^2\ \text{C}$ and a temperature, T_∞, of 24 °C, FEA calculates the steady-state temperature profile within the unit cell topology to be that shown in Fig. 10(*b*). The steady-state temperature at the end of

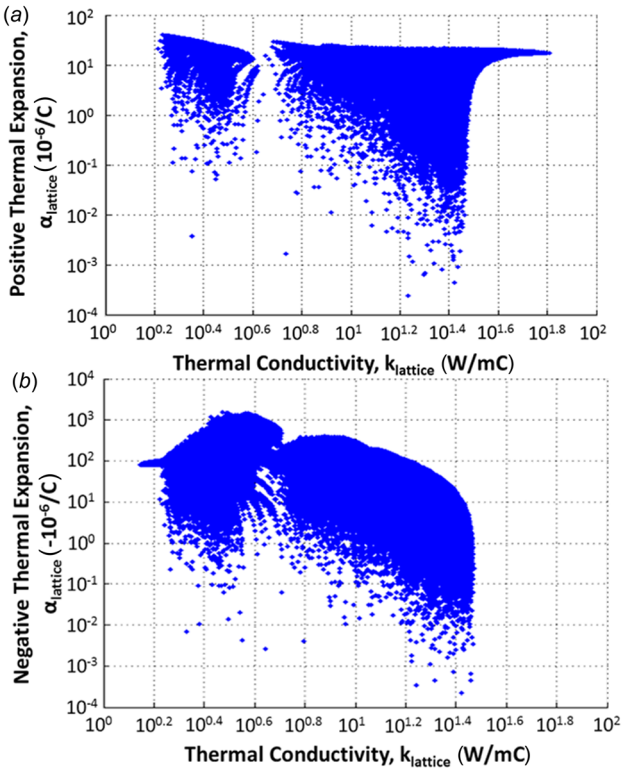

Fig. 9 Positive (*a*) and negative (*b*) thermal expansion versus thermal conductivity

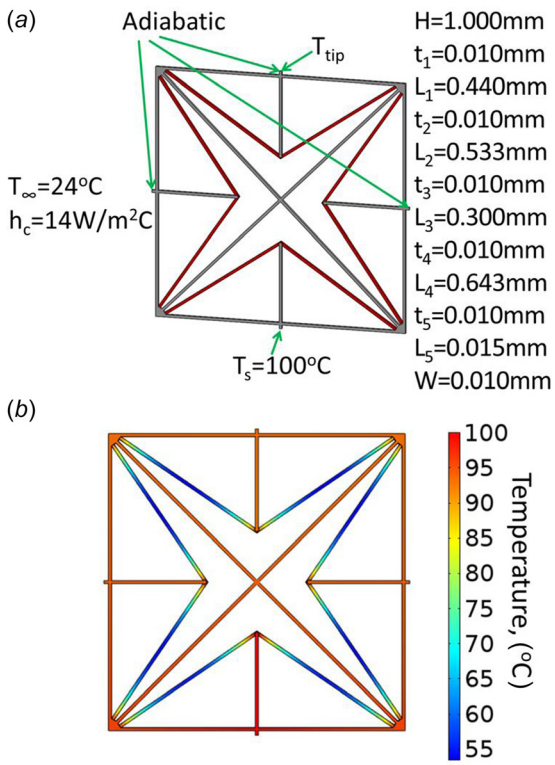

Fig. 10 Unit cell design parameters (*a*) and FEA verification (*b*)

Table 2 FEA verification of the analytical tools of Sec. 3.2

Scale factor	FEA T_{tip} (°C)	Analytical T_{tip} (°C)	Percent error (%)
0.001	99.991	99.99109541	0.0000954223
0.01	99.908	99.91124137	0.003244351
0.1	99.107	99.13901848	0.03230698
1	92.698	92.94022976	0.261310662
10	62.078	62.85696544	1.254817238
100	27.122	27.34261964	0.813434251
1000	24.002	24.00235212	0.001467052

the top tab, T_{tip}, calculated using FEA was compared with the same tip temperature predicted by the analytical tools provided in Sec. 3.2. This comparison was performed for seven different scale factors applied to the same design of Fig. 10(*a*) as shown in Table 2. The results of Fig. 10(*b*) are for a scale factor of 1. Note that the analytical prediction of the top tab's temperature, T_{tip}, is always slightly larger than the FEA calculated temperature because of the analytical method's assumption that the junction bodies possess an infinitely large thermal conductivity. The small percent errors calculated in Table 2 demonstrate how accurate the tools of Sec. 3.2 are for designs with small junction bodies.

5 Conclusions

In this paper, an approach called PSS was introduced that enables designers to correctly insert FACT-synthesized sectors within space-filling polytopes to generate 2D or 3D microstructural architecture topologies that achieve the desired material property directionality (e.g., isotropic, cubic, orthotropic, etc.). Complementary analytical methods are also provided that enable designers to rapidly optimize the geometric parameters of these microstructural architecture topologies such that they achieve specific combinations of thermal expansion coefficients and thermal conductivity values. Using these methods, the achievable material property combinations of general microstructural architecture designs can be plotted within Ashby plots to compare each design's capabilities with the achievable property combinations of natural materials. Tunable thermal expansion 2D and 3D microstructural architecture case studies were synthesized using PSS and fabricated using projection microstereolithography. The analytical methods were used to generate an Ashby plot for one of these synthesized 2D designs. These methods were verified using FEA.

Acknowledgment

This work was performed under the auspices of the U.S. Department of Energy by Lawrence Livermore National Laboratory under Contract DE-AC52-07NA27344. LLNL-JRNL-656139. Support from DARPA's Materials with Controlled Microstructural Architecture program in the Defense Sciences Office, Program Manager Judah Goldwasser, was gratefully acknowledged. We also thank Seth Watts and Daniel Tortorelli at the University of Illinois at Urbana-Champaign for their useful input.

References

[1] Gibson, L. J., and Ashby, M. F., 1997, *Cellular Solids*, Cambridge University Press, Cambridge, UK.
[2] Valdevit, L., Jacobsen, J. A., Greer, J. R., and Carter, W. B., 2011, "Protocols for the Optimal Design of Multi-Functional Cellular Structures: From Hypersonics to Micro-Architectured Materials," J. Am. Ceram. Soc., **94**(s1), pp. s15–s34.
[3] Hopkins, J. B., Lange, K. J., and Spadaccini, C. M., 2013, "Designing Microstructural Architectures With Thermally Actuated Properties Using Freedom, Actuation, and Constraint Topologies," ASME J. Mech. Des., **135**(6), p. 061004.
[4] Ashby, M. F., 2005, *Materials Selection in Mechanical Design*, 3rd ed., Butterworth-Heinemann, Burlington, MA.
[5] Shen, Z., and Hu, G., 2013, "Thermally Induced Vibrations of Solar Panel and Their Coupling With Satellite," Int. J. Appl. Mech., **5**(3), p. 1350031.
[6] Sigmund, O., and Torquato, S., 1996, "Composites With Extremal Thermal Expansion Coefficients," Appl. Phys. Lett., **69**(21), pp. 3203–3205.
[7] Sigmund, O., and Torquato, S., 1997, "Design of Materials With Extreme Thermal Expansion Using a Three-Phase Topology Optimization Method," J. Mech. Phys. Solids, **45**(60), pp. 1037–1067.
[8] Sigmund, O., and Torquato, S., 1999, "Design of Smart Composite Materials Using Topology Optimization," Smart Mater. Struct., **8**(3), pp. 365–379.
[9] Chen, B. C., Silva, E. C. N., and Kikuchi, N., 2001, "Advances in Computational Design and Optimization With Application to MEMS," Int. J. Numer. Methods Eng., **52**(1–2), pp. 23–62.
[10] Lakes, R. S., 1996, "Cellular Solid Structures With Unbounded Thermal Expansion," J. Mater. Sci. Lett., **15**(6), pp. 475–477.
[11] Lehman, J. J., and Lakes, R. S., 2014, "Stiff, Strong, Zero Thermal Expansion Lattices Via Material Hierarchy," Compos. Struct., **107**, pp. 654–663.
[12] Jefferson, G., Parthasarathy, T. A., and Kerans, R. J., 2009, "Tailorable Thermal Expansion Hybrid Structures," Int. J. Solids Struct., **46**(11–12), pp. 2372–2387.
[13] Steeves, C. A., Lucato, S. L., He, M., Antinucci, E., Hutchinson, J. W., and Evans, A. G., 2007, "Concepts for Structurally Robust Materials That Combine Low Thermal Expansion With High Stiffness," J. Mech. Phys. Solids, **55**(9), pp. 1803–1822.
[14] Yamamoto, N., Gdoutos, E., Toda, R., White, V., Manohara, H., and Daraio, C., 2014, "Thin Films With Ultra-Low Thermal Expansion," Adv. Mater., **26**(19), pp. 3076–3080.
[15] Collishaw, P. G., and Evans, J. R. G., 1994, "An Assessment of Expressions for the Apparent Thermal Conductivity of Cellular Materials," J. Mater. Sci., **29**(9), pp. 2261–2273.
[16] Boetes, R., and Hoogendoorn, C. J., 1987, "Heat Transfer in Polyurethane Foams for Cold Insulation," International Symposium on Heat and Mass Transfer in Refrigeration and Cryogenics, International Centre for Heat and Mass Transfer Digital Library, pp. 14–31.
[17] Glickman, L., Schuetz, M., and Sinofsky, M., 1987, "Radiation Heat Transfer in Foam Insulation," Int. J. Heat Mass Transfer, **30**(1), pp. 187–197.
[18] Hashin, Z., and Shtrikman, S., 1962, "A Variational Approach to the Theory of the Effective Magnetic Permeability of Multiphase Materials," J. Appl. Phys., **33**(10), pp. 3125–3131.
[19] Carson, J. K., Lovatt, S. J., Tanner, D. J., and Cleland, A. C., 2005, "Thermal Conductivity Bounds for Isotropic, Porous Materials," Int. J. Heat Mass Transfer, **48**(11), pp. 2150–2158.
[20] Evans, A. G., Hutchinson, J. W., Fleck, N. A., Ashby, M. F., and Wadley, H. N. G., 2001, "The Topological Design of Multifunctional Cellular Metals," Prog. Mater. Sci., **46**(3–4), pp. 309–327.
[21] Tian, J., Kim, T., Lu, T. J., Hodson, H. P., Queheillalt, D. T., Sypeck, D. J., and Wadley, H. N. G., 2004, "The Effects of Topology Upon Fluid-Flow and Heat-Transfer Within Cellular Copper Structures," Int. J. Heat Mass Transfer, **47**(14–16), pp. 3171–3186.
[22] Hopkins, J. B., 2013, "Designing Hybrid Flexure Systems and Elements Using Freedom and Constraint Topologies," Mech. Sci., **4**(2), pp. 319–331.
[23] Cowin, S. C., and Mehrabadi, M. M., 1995, "Anisotropic Symmetries of Linear Elasticity," ASME Appl. Mech. Rev., **48**(5), pp. 247–285.
[24] Lakes, R., 2007, "Cellular Solids With Tunable Positive or Negative Thermal Expansion of Unbounded Magnitude," Appl. Phys. Lett., **90**(22), p. 221905.
[25] Crandall, S. H., Dahl, N. C., and Lardner, T. J., 1999, *An Introduction to the Mechanics of Solids*, 2nd ed., McGraw-Hill, New York.
[26] Sun, C., Fang, N., Wu, D. M., and Zhang, X., 2005, "Projection Micro-Stereolithography Using Digital Micro-Mirror Dynamic Mask," Sens. Actuators, A, **121**(1), pp. 113–120.
[27] Zheng, X., Deotte, J., Alonso, M. P., Farquar, G. R., Weisgraber, T. R., Gemberling, S., Lee, H., Fang, N. X., and Spadaccini, C. M., 2012, "Design and Optimization of a Light-Emitting Diode Projection Micro-Stereolithography Three-Dimensional Manufacturing System," Rev. Sci. Instrum., **83**(12), p. 125001.
[28] Ball, R. S., 1900, *A Treatise on the Theory of Screws*, Cambridge University Press, Cambridge, UK.
[29] Incropera, F. P., and DeWitt, D. P., 2002, *Fundamentals of Heat and Mass Transfer*, 5th ed., Wiley, New York.